



HAL
open science

Experiments on grain size segregation in bedload transport on a steep slope

P. Frey, H. Lafaye de Micheaux, C. Bel, Raphaël Maurin, K. Rorsman, T. Martin, Christophe Ducottet

► **To cite this version:**

P. Frey, H. Lafaye de Micheaux, C. Bel, Raphaël Maurin, K. Rorsman, et al.. Experiments on grain size segregation in bedload transport on a steep slope. *Advances in Water Resources*, 2020, 136, pp.103478. 10.1016/j.advwatres.2019.103478 . ujm-02453772

HAL Id: ujm-02453772

<https://ujm.hal.science/ujm-02453772>

Submitted on 26 Feb 2021

HAL is a multi-disciplinary open access archive for the deposit and dissemination of scientific research documents, whether they are published or not. The documents may come from teaching and research institutions in France or abroad, or from public or private research centers.

L'archive ouverte pluridisciplinaire **HAL**, est destinée au dépôt et à la diffusion de documents scientifiques de niveau recherche, publiés ou non, émanant des établissements d'enseignement et de recherche français ou étrangers, des laboratoires publics ou privés.



Open Archive Toulouse Archive Ouverte

OATAO is an open access repository that collects the work of Toulouse researchers and makes it freely available over the web where possible

This is an author's version published in: <https://oatao.univ-toulouse.fr/27464>

Official URL:

<https://doi.org/10.1016/j.advwatres.2019.103478>

To cite this version:

Frey, Philippe and Lafaye de Micheaux, Hugo and Bel, Coraline and Maurin, Raphaël  and Rorsman, Kristina and Martin, T. and Ducottet, Christophe
Experiments on grain size segregation in bedload transport on a steep slope.
(2020) *Advances in Water Resources*, 136. 103478. ISSN 0309-1708.

Any correspondence concerning this service should be sent
to the repository administrator: tech-oatao@listes-diff.inp-toulouse.fr

EXPERIMENTS ON GRAIN SIZE SEGREGATION IN BEDLOAD TRANSPORT ON A STEEP SLOPE

P. Frey^{*,a}, H. Lafaye de Micheaux^{a,b}, C. Bel^a, R. Maurin^c, K. Rorsman^a, T. Martin^a,
C. Ducottet^b

^aUniv. Grenoble Alpes, Irstea, UR ETNA, 38000 Grenoble, France

^b Université de Lyon, UJM-Saint-Etienne, CNRS, IOGS, Laboratoire Hubert Curien UMR5516, F-42023, Saint-Etienne, France

^cInstitut de Mécanique des Fluides de Toulouse, Univ. Toulouse, CNRS, 31400 Toulouse, France

*Corresponding author: Irstea, UR ETNA, 2 rue de la Papeterie-BP 76, 38402 St-Martin-d'Hères, France
e-mail address : philippe.frey@irstea.fr

KEYWORDS

Sediment transport, bedload, experimental, segregation, two-phase flow, granular flow,
particle tracking

ABSTRACT

Sediment transport in mountain and gravel-bed-rivers is characterized by bedload transport of a wide range of grain sizes. When the bed is moving, dynamic void openings permit downward infiltration of the smaller particles. This process, termed here ‘kinetic sieving’, has been studied in industrial contexts, but more rarely in fluvial sediment transport. We present an experimental study of two-size mixtures of coarse spherical glass beads entrained by turbulent and supercritical steady water flows down a steep channel with a mobile bed. The particle diameters were 4mm and 6mm, and the channel inclination 10%. The spatial and temporal evolution of the segregating smaller 4mm diameter particles was studied through the introduction of the smaller particles at a low constant rate into the large particle bedload flow at transport equilibrium. Particle flows were filmed from the side by a high-speed camera. Using original particle tracking algorithms, the position and velocity of both small and large particles were determined. Results include the time evolution of the layer of segregating smaller beads, assessment of segregation velocity and particle depth profiles. Segregation resulted in the progressive establishment of a quasi-continuous region of small particles reaching a steady-state penetration depth. The segregation dynamics showed a logarithmic time decreasing trend. This evolution was demonstrated to be dependent on the particle streamwise shear rate which decays downwards exponentially. This result is comparable to theories initially developed for dry granular flows.

1. INTRODUCTION

Flooding hazards, reproduction of salmonids, earth landscapes are all heavily impacted by sediment transported by rivers. Yet, after more than a century of research (DuBoys, 1879; Gilbert, 1914), there is no satisfactory theory available for sediment transport, especially for bedload, the coarser sediment load transported in contact with the stream bed. Empirical sediment rate formulas often poorly compare with field measurements by sometimes orders of magnitude (Gomez and Church, 1989; Hinton et al., 2018). An important factor impairing our ability to predict sediment transport is the wide range of grain sizes within bedload, leading to size segregation, also known as grain size sorting. This phenomenon drastically modifies fluxes and results in patterns that can be seen ubiquitously in nature, such as armoring (Bathurst, 2007). This is particularly the case in mountain streams where steep slopes drive an intense transport of a wide range of grain sizes. In this paper, focus lies on vertical size segregation with controlled laboratory experiments using idealized spherical particles within a steep narrow flume.

Two distinct size segregation phenomena occur, both relevant to bedload flows, whether the coarsest fractions of the bed are immobile or not: ‘spontaneous percolation’ and ‘kinetic sieving’ respectively. ‘Spontaneous percolation’, the size segregation by infiltration of fine sediment into an immobile gravel or boulder bed (Bridgwater and Ingram, 1971) has been extensively studied in fluvial geomorphology. There have been diverse motivations to study the phenomena including the intrusion of fines into salmonid spawning beds, placer mineral concentration, and stratigraphical interpretation. Research has been undertaken experimentally (Beschta and Jackson, 1979; Dermisis and Papanicolaou, 2014; Dudill et al., 2017; Einstein, 1968; Gibson et al., 2011), in the field (Frostick et al., 1984; Lisle, 1989) and using models (Cui et al., 2008). Spontaneous percolation, essentially by the effect of gravity, can only occur

for sufficiently high size ratios (large to fine diameter) depending predominantly on the grain size distribution and on the shape of the material.

However, when the coarse bed is moving, another type of segregation can take place even with a size ratio close to unity. The moving bed acts as a sieve, in which smaller particles are more likely to fall into gaps opened by shearing. The typical net result is a downward flux of the smaller particles and an upward flux of larger particles, causing vertical reverse segregation.

This gravity- and shear-driven phenomenon has been variously termed kinetic sieving (Middleton, 1970), interparticle percolation (Drahn and Bridgwater, 1983) or gravity-driven segregation (Gray, 2018). It has been significantly studied in the powder and grain community concerned with industrial applications. A landmark paper (Savage and Lun, 1988) proposed a model resulting from the combination of a ‘random fluctuating sieve’ mechanism and ‘squeeze expulsion’ whereby particles are squeezed upwards out of a layer. The term ‘kinetic sieving’ sometimes seems to be used somewhat restrictively to refer only to the model by Savage and Lun (1988). We will, however, use this colorful term to describe the entire shear driven reverse segregation phenomenon instead of a specific model.

Kinetic sieving in stream channels has rarely been highlighted despite its morphodynamic relevance, though to the best of our knowledge this term was coined by a geologist (Middleton, 1970). Note, however, that Parker and Klingeman (1982) described the process as ‘vertical winnowing’ whereby small grains fall into holes created by the movement of the larger grains in the armored river bed surface. Accordingly, we focus on kinetic sieving in the present contribution.

Kinetic sieving has been studied experimentally in dry granular inclined chute flows (Savage and Lun, 1988; van der Vaart et al., 2015; Wiederseiner et al., 2011). The theory (Savage and Lun, 1988) evidenced a dependency of the segregation rate on the shear rate. Other theories rely on the kinetic theory of gases (Fan and Hill, 2011) and mixture models have been proposed

(Gajjar et al., 2016; Thornton et al., 2006; Tunuguntla et al., 2014). Although the effect of interstitial fluid on granular flow properties has received attention (Jain et al., 2004; Thornton et al., 2006), segregation in bedload transport which is a granular flow shear-driven by a free surface water flow has rarely been investigated (Ferdowsi et al., 2017).

In the laboratory at Irstea, a very efficient vertical and longitudinal sorting process was evidenced with bed sample measurements during bedload transport experiments on steep slopes with natural material mixtures (Bacchi et al., 2014; Recking et al., 2009b). Subsurface fining occurred which was attributed to kinetic sieving. Dudill et al. (2017, 2018) also performed experiments with spherical glass beads with a large range of grain size ratios (ratio of large to fine diameter). They found that below a ratio of 1.7, no spontaneous percolation occurred, only kinetic sieving. Furthermore, kinetic sieving excluding spontaneous percolation was first qualitatively investigated at Irstea by Frey and Church (2009) and Hergault et al. (2010) in the same quasi-2D flume that will be used and described herein.

Considering the importance of kinetic sieving for morphodynamics, poor characterization and understanding of the underlying physical processes, the aim of the present research is to investigate size segregation in turbulent bedload transport with the help of high resolution experiments. Thanks to innovative quantitative image analysis measurements, the granular depth structure can be analyzed (Frey, 2014; Revil-Baudard et al., 2015), allowing for a better process understanding, exploring in particular the link between segregation and the shear rate. Such an unique dataset is also of high importance for the validation of refined numerical models either in the continuum (Chauchat, 2018; Cheng et al., 2018) or in the discrete framework (Maurin et al., 2015).

2. EXPERIMENTAL METHODS

2.1 *Experimental arrangement*

Experiments were carried out in the narrow two meter long sediment-feed flume hosted at the National Research Institute of Science and Technology for Environment and Agriculture (Irstea) located in the University Grenoble Alpes campus, France (Figure 1). The width of the channel was 6.5 mm and the slope ‘S’ 10 % (5.7°). Uncertainty of the slope was ± 0.1 %. A steady water flow rate was ensured by a constant head reservoir and controlled with an electromagnetic flow meter (less than 1% uncertainty).

Figure 1 : Set-up of the experimental device (modified from Hergault et al. 2010). The x-y coordinate system is shown. Note that the origin is taken at the top of the downstream obstacle

Two types of spherical glass particles were used each with a density of $2,500 \text{ kg/m}^3$. The larger particles were black with a diameter $D = 6 \pm 0.3 \text{ mm}$ (provided by Sigmund Lindner GmbH, Germany) and the smaller ones were transparent with a diameter $d = 4 \pm 0.3 \text{ mm}$ (provided by CIMAP, France).

As the flume is only slightly wider than the diameter ‘D’ of the large beads, it allows for a quasi-2D movement to occur and greatly facilitate particle tracking. Numerical simulations have shown that the granular flow structure and fluid-particle coupling observed in such a quasi 2D configuration exhibit the same mechanisms and signatures to that observed in full 3D configurations (Maurin et al., 2015). This supports the relevance of the experimental setup, in particular for the present analysis focusing on the granular behavior. To prevent crystallographic-type arrangements of spheres within the bed, the flume has a steel bottom made of cylinders of the same diameters as the large beads and located at random heights. A 40 mm high obstacle was positioned at the downstream end of the flume so as to permit bed formation

of about 6-7 layers of large beads. The origin of the elevation y was taken at the top of this obstacle (Figure 1) and the elevation normalized by the large diameter D will be denoted y^* .

The procedure to obtain transport equilibrium with the large beads followed several steps. First, the large glass beads were injected at the desired rate from a reservoir with a motorized wheel equipped with 20 hollows on its circumference. The feed rate was constant within 4%. The water supply was subsequently adjusted to make the bed line parallel to the channel base. Finally, we ensured that transport equilibrium was reached. By transport equilibrium, we mean that the outgoing sediment rate was equal to the input rate and that there was no more aggradation nor degradation (i.e. no positive or negative change of the bed slope) over a sufficiently long time interval. The outflowing sediment rate was monitored for approximately 20 minutes to ensure that the transport equilibrium condition was respected. The outgoing sediment rate was measured during 1 minute at least three times during the 20 minute period. If these three values were consistently equal to the ingoing sediment rate within 8%, transport equilibrium was assumed.

We focused in this study on both a low and a high flow discharge experiment with a feed rate of approximately 6 and 20 large beads/s (0.10l/s/m and 0.35l/s/m). These experiments will hereafter be defined as S6 and S20.

When the above procedure was successfully completed, the smaller transparent beads were input upstream of the recorded image field at a very low rate of one bead every two seconds ($2.58 \cdot 10^{-3}$ liter/s/m) to study the vertical segregation process. The sediment rate of small beads was chosen sufficiently low (only 2.5% of the rate of large beads for S6 and less than 1% for S20) to preserve transport equilibrium: no significant change of the slope was subsequently observed nor adjustment of the flow rate necessary.

2.2 Experimental parameters

We give in table 1 all relevant hydrodynamic and sedimentological parameters. The sediment transport rate imposed at the inlet is given both in absolute experimental values (\dot{n}_0 in beads/s) and per unit width (q_s in m^2/s). q_w is the flow rate per unit width.

The water depth, h , was obtained from the water free surface and bed surface detections by image processing (see details in next subsection). The water depth fluctuated significantly over the experiment duration and along the main stream direction. For data calculated over a duration of 0.2s, the standard deviation was 0.7 mm. In Table 1, the water depth is averaged over time and space. All subsequent parameters in table 1 are calculated from the water depth.

$\overline{u_f} = \frac{q_w}{h}$ is the mean fluid velocity.

The Froude number is defined as $Fr = \frac{\overline{u_f}}{\sqrt{g \cdot h}}$ (where g denotes gravity acceleration).

Using the so-called Einstein (1942) sidewall correction, flow dissipation by the smooth sidewalls was taken into account by calculating a bottom hydraulic radius Rh_b . The method is explained in (Frey et al., 2006). This allowed us to assess a more consistent Shields number

$\theta_b = \frac{Rh_b \cdot S}{(s-1) \cdot D}$ than if it were calculated with the water depth ($s = \rho_s/\rho = 2.5$ is the ratio of sediment to water density).

The flow was turbulent (Reynolds number above 4,000) and hydraulically rough. The steep slope of the flume meant that the flow was supercritical (Froude number of 1.2-1.3) and that the submergence h/D (the ratio of flow depth to the particle diameter) was low at 1.6 and 2.8. Despite these unusual conditions, the water flow in this flume, has been shown still to behave classically as in larger flumes, in particular with the presence of a logarithmic layer (Frey and

Reboud, 2001). Moreover one–size sediment rates have been shown to be in good agreement (Dudill et al., 2017) with classic semi-empirical bedload formulae such as Meyer-Peter and Müller (1948).

The Shields number ranged from 0.081 to 0.115. This is about two times the classical incipient motion value. As all beads moved frequently, with only some periods of rest, the flow can be classified in stage 3 (Warburton, 1992) or termed ‘full mobility bedload’ (Frey and Church, 2011). However, the flow was well below the intense bedload range depicted by Capart and Fraccarollo (2011).

Experiments	S6	S20
\dot{n}_0 (beads/s)	5.9	19.7
q_s ($10^{-3}\text{m}^2/\text{s}$)	0.104	0.343
q_w ($10^{-3}\text{m}^2/\text{s}$)	3.62	8.65
h (mm)	9.6	16.9
\bar{u}_f (m/s)	0.38	0.51
Rh_b (mm)	7.3	10.4
Fr	1.22	1.26
h/D	1.6	2.8
θ_b	0.081	0.115

Table 1: Bedload and water flow characteristics. See text for notations.

2.3 Image acquisition

All experiments were recorded using a Baumer HXC13 high-speed camera. The camera was positioned perpendicular to the sidewalls, approximately 90 cm upstream from the channel outlet and inclined at the same angle as the channel (Figure 1). A high bright white LED backlight panel was positioned behind the channel and provided stable and uniform lighting. The camera recorded at a rate of 130 frames per second, and the image resolution was 1280 x 320 pixels, which corresponds approximately to a window of 260mm by 65mm. Up to 500,000 images were recorded over one hour (images are shown in Figure 3).

Preliminary test runs showed that a duration of about one hour was sufficient for S6 and 45 min for S20 to obtain a steady state segregation pattern characterized by a quasi-continuous region of small beads.

Figure 3f and Figure 3l display an image of each run at a time near the end of the experiment when the steady state segregation pattern had been reached (see also phenomenological descriptions in section 3).

In preliminary tests, the smaller beads were input exactly at the upstream corner of the recorded image field of view. Beads then began to saltate and roll. The majority of the introduced beads never infiltrated into the bed and rapidly left the field of view. Some beads, however, were caught in the bed and infiltrated immediately downstream of the feeder position. At steady state, a region with only a very low number of infiltrated small beads could be identified between the feed location and the upstream position of the quasi-continuous layer. The length between this position, which fluctuated somewhat with time, and the feed location could be estimated to approximately 10D for S6 (see Figure 3f) and 35D for S20. For context, the total length of the image field of view is 44D. As a result, in run S20, the quasi-continuous region had a length of only 9D which meant insufficient small beads in the field of view to perform any consistent statistics. Therefore, for the higher rate run S20, we

decided to input the smaller beads upstream of the upper left corner at a distance of 44D which yielded a quasi-continuous small bead region over the entire image (see Figure 3l). This was not necessary for run S6 since the quasi-continuous region was larger with a sufficient number of infiltrated small beads (see Figure 3f).

2.4 Image processing

Thanks to a sufficient resolution and frame rate, acquired sequences of images contain enough information to extract the trajectories of individual beads. The algorithm to obtain the individual trajectory of each object relies on a two-step deterministic approach: 1. object detection, 2. object tracking from frame to frame (Hergault et al., 2010; Lafaye de Micheaux et al., 2018). In parallel, characteristic lines such as the water free surface and bed surface can be automatically detected thanks to segmentation methods with a dedicated image processing chain (Lafaye de Micheaux et al., 2018; Lafaye de Micheaux et al., 2015). All the algorithms coded in Matlab are included in a package called *BeadTracking* available on <https://github.com/hugolafaye/BeadTracking>. Moreover, a ground truth consisting of a 1000-frame experimental image sequence was used for validation and is available on Zenodo <https://doi.org/10.5281/zenodo.3454628>. The entire trajectory dataset for both runs S6 and S20 is available on <https://doi.org/10.5281/zenodo.3407127>. In addition 18 sequences of raw images corresponding to data used in figure 5 are also included (9 sequences for run S6 and 9 sequences for run S20).

2.4.1 Object detection

For each image, the object detection phase aims at detecting all beads (Figure 2a) by image processing. First, black large beads are detected by thresholding the image to keep only black

pixels (Figure 2b), eroding to isolate black beads (Figure 2c) and then identifying the center of connected components (Figure 2d). This detector is very efficient since black beads are not overlapping and are easily distinguishable from other kind of beads (6 mm diameter beads in a channel width of 6.5 mm). It returns the set of black bead centers. Then, black beads are erased by replacing their gray levels by those of the background (Figure 2e). The background is reconstructed through a morphological closing with a disc shaped structuring element (radius just greater than bead radius). This makes transparent beads more discernible. Secondly, since transparent beads appear as faint dark rings of different shapes because of their neighboring configurations (4 mm diameter beads can be partially overlapped by others), we use a specific chain of morphological operations to detect them (initially developed by Hergault et al. (2010)). We apply a *hconvex* operator (Soille, 1999) on the image obtained at the previous step (Figure 2f), then a normalized cross-correlation with a ring-shaped model (Figure 2g), local maxima extraction and maxima selection according to an adjusted threshold (Figure 2h). This returns the set of transparent bead centers.

Figure 2 Steps of the object detection process. (a) original image, (b) thresholding to keep only black pixels, (c) eroding to isolate blacks beads, (d) detecting the center of the individual connected components being the black bead centers, (e) erasing black beads, (f) transforming by *hconvex*, (g) correlating with a ring-shaped model, (h) selecting maximal correlation results as being the transparent bead centers.

2.4.2 Object tracking

To assign at most one detection to at most one tracker (*i.e.* each physical trajectory is estimated by an individual internal state called ‘tracker’), a detection-tracker association process is needed. Due to the high number of detections and the long time series, the association was done deterministically with a greedy algorithm (Wu and Nevatia, 2007).

Given the matching cost between all possible detection-tracker pairs, the greedy algorithm iteratively selects the best candidate and removes the corresponding concurrent associations.

The matching cost between a detection and a tracker consists of a combination of two factors:

one based on the distance from the detection position to the predicted position of the tracker, the other based on the tracker velocity at the previous time step. The distance term promotes the detections closest to the prediction. With the velocity term, we promote low velocities as it allows better associations in case of bead collisions. Indeed, when a bead bounces, its predicted position (assuming a constant velocity model) can fall very close to another bead leading to the same distance term for the corresponding trackers. In this case, adding a velocity term to the matching cost increases the cost of higher velocities much more than lower ones, and so favors choosing lower velocities first during the greedy data association.

To limit the number of possible detection–tracker pairs, the set of possible detections associated to a given tracker is limited to the detections located inside a circular region centered at the predicted position given by this tracker. This predicted position is determined assuming a constant velocity model. In the end, the tracking algorithm returns the set of estimated trajectories over the sequence of images. Examples of trajectories are given on Figures 2*b* and 2*f*.

2.4.3 *Water surface and bed line detection*

Both water free surface and bed surface detections are based on a combination of image analysis techniques such as morphological operations, gradient calculations and watershed transformations (Beucher and Lantuejoul, 1979; Vincent and Soille, 1991). The water free surface is detected by first removing detected beads, then amplifying it by *bottom-hat* filtering, and then applying a marker-controlled watershed, to finally return the water free surface as a thin line. The bed surface is detected by first computing the average image over N consecutive images removed from their detected water free surface, then computing a gradient magnitude of the obtained image, and then applying a marker-controlled watershed, to finally return the bed surface as a thin line. These detected lines allowed the derivation of water depth as the difference between the water free surface and the bed line.

2.5 Post processing

Results of both the center location and the velocity of each bead are used to compute the depth profiles. We partition each image into equally sized bins parallel to the x streamwise direction, comprising the entire length of the image and the thickness of n pixels in the normal direction. The procedure is similar to that of Hill and Fan (2008) and Maurin et al. (2015).

For each elevation, the volumetric solid concentration C is computed as the sum of all volume portions of beads present in the bin V_s divided by the total volume of the bin V . V_s is simple to calculate since the volume of a slice of a sphere can be evaluated analytically. The average particle velocity U_p is computed similarly with the velocity of each bead weighted by its portion present in the bin. Averaging is made over all images within a considered temporal sequence.

Using a bin of thickness 1 pixel resulted in too noisy profiles. Testing with larger bins from 30 pixels down to 1 pixel showed that a bin of 15 pixels (half the diameter of a large bead) ensured a readable and still converging profile. Particular attention was paid to ensure that the spatial gradients were still preserved.

The particle transport rate per unit width at each elevation was defined as $q_s = U_p \cdot C$ ($\text{m}^2/\text{s}/\text{m}$).

We defined the bedload layer as all elevations exhibiting a particle transport rate higher than 2% of its maximum value.

We seek to follow the temporal evolution of the segregation pattern. To achieve this, we need to choose temporal sequences comprising a sufficient number of images. This allows us to reach statistical consistency but the sequence should not be too long to ensure a small variation of variables within the sequence. Temporal sequences were chosen with a number of images between 8,000 and 10,000 (corresponding to a duration of 61s to 77s). In the legend of figures, the median time is used to label the temporal sequences. The initial time, 0, is defined as the time when the first small bead was introduced.

3. RESULTS

3.1 Phenomenology

Figure 3 Sequence of images showing the temporal evolution of the segregation patterns in run S6 (a-f) and run S20 (g-l). Superimposed trajectories appear on panel b (over a prior duration of 38s) and f (over a prior duration of 6 min only for beads still present in the image).

Before giving quantitative results, we will describe the qualitative evolution of both runs S6 and S20, with the help of sequences of images (Figure 3).

While the majority of introduced small beads saltate and leave the downstream end of the image, some beads infiltrate through the large beads by kinetic sieving. They tend to form clusters very rapidly though some rare beads remain isolated (see Figure 3b and Figure 3h for both runs at 138s). The number and the size of these clusters increase (see Figure 3c and Figure 3i for both runs at 600s) before progressively merging to form a quasi-continuous layer of small beads (see run S6 at 1522s and 2509s, Figure 2d and e; and run S20 at 1200 and 1800s, Figure 2j and k). The evolution is then slower before reaching a dynamic steady-state final segregation pattern (see Figure 3f and Figure 3l for S6 and S20). In neither run did any bead reach the steel bottom. At the final stage the elevation of the bottom of the small bead layer does not seem to vary any more. This elevation, that we will call ‘penetration depth’, is clearly identifiable and depends on the run considered. A higher penetration depth is observed for S20 with a larger sediment rate corresponding to a higher Shields number. We will analyze below this important feature with the help of concentration profiles.

Once infiltrated in the bed, most small beads remained trapped during the entire experiment. However, the shear-driven general movement meant that some beads in the upper layers could be re-caught in the bedload layer and finally disappear from the image. Shearing also meant

that several beads could progressively disappear or appear through the downstream or upstream edge of the image field.

3.2 Initial one-size depth structure

Figure 4 : Depth structure of the initial one-size bedload flow (black square for S6 and red diamond for S20) a) particle velocity (with semi-log inset showing exponential decay) b) solid volume concentration c) particle transport rate

We recall here the principal characteristics of the depth structure, once transport equilibrium is established, for flows composed only of one size of the large beads. More details can be found in Frey et al. (2014).

Figure 4 gives the depth profiles of the particle velocity, the volumetric solid concentration and the particle rate for both S6 and S20. The velocity profile is characterized from bottom to top by an exponential decay, a linear part and a logarithmic-like region. The velocity of S20 is always higher than that of S6 at all elevations.

In the bed the solid concentration is maximal with a mean value of about 0.53. Some oscillations are reminiscent of a layered structure. Above $y^* = 0$, i.e. above the top of the downstream obstacle, there is a dramatic decrease up to the free surface. From $y^*=0$ to 1 the concentration is smaller for S20 than for S6. Above $y^*=1$ it is the reverse due to a higher number of beads in saltation for S20.

The sediment rate is the product of velocity and concentration as defined in postprocessing. In our case, when the concentration is low, the velocity is high and vice versa. The sediment rate peaks around $y^*=1$ for both runs and has an approximate Gaussian shape though skewed downwards. The bedload layer, as defined above, with values of sediment rate larger than 2% of its maximum value, ranged from $y^* = -1$ to 2.5 for run S6 and from -2 to 2.8 for run S20.

The region below the bedload layer is characterized by low particle velocities, hence the use of the term ‘quasi-static’ flow or ‘creeping’ flow (Houssais et al., 2015). Since particle velocities are small in this region, it does not practically contribute to the bedload rate. However the properties of this region are of utmost importance for the evolution of vertical segregation. Of particular interest is the exponential decay of the particle velocity (see inset of Figure 4) and hence of the shear rate (gradient of the velocity). The consequences of this interesting property will be used in the discussion section where a link between segregation and shear rate will be evidenced.

3.3 Concentration profiles of small particles

Figure 5 shows the time evolution of small bead concentration profiles for both runs S6 and S20. The concentration x-axis scale is the same and the y-axis depicts a range of 5.5 diameters below $y^*=1$ for run S6 and below 0 for run S20 (same range with a translation of 1D).

Figure 5 Temporal evolution of the small particle volume concentration depth profiles a) run S6 b) run S20. The median time of the temporal sequence is used in the legend. Axis scaling is the same but note a translation of 1 diameter D on the y-axis from S6 (-4.5 to 1) to S20 (-5.5 to 0)

The same shape can be observed for both runs. The concentration profiles are quasi-Gaussian though skewed towards the bottom. Right from the beginning and at all times, the profile of S20 peaks at a lower elevation than S6. At the final stage the profile of S20 is slightly thicker than S6 (approximately 4D vs. 3.5D).

Looking at the time evolution on Figure 5 (see also

Figure 3 with the images), there is a decrease of the peak vertical position, relatively sharp for S20, more diffuse for S6. There is clearly a rapid increase of concentration in the lowest layers. In both runs it is remarkable that the lowest limbs approximately collapse onto a single curve.

This behavior, related to the penetration depth, will now be analyzed in more details with the help of concentration isolines.

3.4 Concentration isolines

Figure 6 shows for the two runs the concentration isolines in the elevation-time space. Each isoline corresponds to a constant concentration value chosen as: 0.01, 0.02, 0.05, and 0.1. For each concentration value, there is a lower and an upper isoline (hence 2 series of 4 curves on each graph). In both runs, the lower isolines decrease with time, first sharply then more gradually for finally reaching a steady penetration depth. By contrast, the upper isolines are more or less horizontal, showing no trend. Comparing globally the upper isolines, it is observed that in run S20 they are located 1 diameter below those of run S6. And for the lower isolines, this difference is approximately 1.5 diameter.

At final steady state, for instance at a concentration of 0.02, the upper and lower isolines are around $y^* = 0$ and -3.25 for S6, and around $y^* = -1$ and -5 for S20, which results in a thickness of respectively $3.25D$ and $4D$. For a concentration of 0.05, the upper and lower isolines are around $y^* = -0.5$ and -3 for S6, and around $y^* = -1.5$ and -4.5 for S20, which makes a thickness of respectively $2.5D$ and $3D$. So, these figures also indicate a slightly larger thickness of the small bead region for S20.

Figure 6 : Upper and lower isolines of concentration for constant values of 0.01, 0.02, 0.05 and 0.1 a) run S6 b) run S20. Axis scaling is the same but note a translation of 1 diameter D on the y-axis from S6 (-4.5 to 1) to S20 (-5.5 to 0)

Clearly, the evolution of the lower isolines is very dynamic at the beginning. Figure 7 shows a semi-log plot of the temporal evolution of each lower isoline.

Figure 7 Lower isolines of Concentration for constant values of 0.01, 0.02, 0.05 and 0.1 (from bottom to top) showing a logarithmic time evolution until about 1,000s. A best fit is plotted for 0.01, 0.02 and 0.05 isolines a) run S6 b) run S20. Axis scaling is the same but note a translation of 1 diameter D on the y-axis from S6 (-4.5 to -1) to S20 (-5.5 to -2)

In run S20, a logarithmic time decreasing trend is observed for all lower isolines up to a time between 1,000 and 2,000s. It is particularly obvious for $C=0.01$ and 0.02 . In run S6, the logarithmic time decreasing trend is also observed but less obviously. More quantitatively, we have fitted the experimental isolines with logarithmic curves for the 3 cases $C=0.01, 0.02, 0.05$, a being the absolute slope value of the fitted line and b the y -intercept:

$$y_c^* = -a \log(t) + b \quad (1)$$

Table 2 gives the fitted values for each concentration isoline and for both runs, together with the coefficient of determination.

	S6			S20	
Isolines	Slope a	R^2	Slope a	R^2	
C=0.01	1.23	0.94	1.95	0.98	
C=0.02	1.21	0.97	2.09	0.99	
C=0.05	1.37	0.87	2.13	0.98	

Table 2: best fit result of the logarithmic concentration isolines. The absolute slope value a (see eq. 1) together with the coefficient of determination, R^2 , is given for the three values of concentration (0.01, 0.02 and 0.05) for both experiments S6 and S20 (see Figure 7)

Run S20 with a higher Shields number displays larger absolute slope values ranging from 1.95 to 2.13 denoting a faster segregation rate than run S6 ranging from 1.21 to 1.37. For both runs, regardless of the concentration ($C=0.01, 0.02$ and 0.05), the slope of the isolines is very similar, which is remarkable.

3.5 Normal small particle velocity

Figure 8 Temporal evolution of normal small particle velocity depth profiles a) run S6 b) run S20. The median time of the temporal sequence from time 0 is used in the legend.

Image analysis allows us to track each bead and thus to compute the normal small particle velocity, i.e. orthogonal to the bed slope, which is on average negative since kinetic sieving implies an average downward movement. In Figure 8 where the absolute downward velocity $|U_{p_y}|$ is plotted, we focus on the dynamic evolution taking place until about 500-600s (see Figure 3c and i).

For all elevations, the downward velocity of run S20 is noticeably higher than for run S6. For both runs, S6 and S20 and for all time sequences, the downward velocity decreases sharply in the dynamic layer between $y^* = 1$ and about $y^* = 0$, then more gradually in the region between $y^* = 0$ and $y^* = -1.5$.

At initial times, the downward velocity is significant in the region around $y^* = 0$ (S6) and -1 (S20). Then, it approaches zero at later times.

More specifically, in run S20 the mean downward velocity decreases to $1.5 \cdot 10^{-4}$ m/s at an elevation of $y^* = -1.5$ at time 138s (brown curve) whereas the same velocity is reached at a higher elevation of about -0.5 at the later time of 576s (magenta curve). In run S6, this time evolution can also be observed though less clearly. For example, at $y^* = 0$, the velocity has a mean value of $3 \cdot 10^{-4}$ m/s at 64s, dropping to $0.15 \cdot 10^{-4}$ m/s at 495 s. The intermediate profiles display a value of about 10^{-4} m/s.

Essentially, the velocity tends to approach 0 at a higher elevation as time increases and as the quasi-continuous small bead layer is building (see Figure 3 displaying the temporal evolution of the images).

An assumption is that this behavior is controlled by the dynamic conditions prevailing at the bottom of this quasi-continuous layer, notably by the shear rate behavior. Since the normal motion of the bottom of the evolving quasi-continuous small bead region progressively decreases, the normal movement of beads located above becomes hindered and hence the downward small particle velocity in the upper layers tends to decrease as evidenced in Figure 8. We will explore this assumption further in the following discussion section.

4. DISCUSSION

4.1 Shear rate dependence

To discuss the time evolution of the concentration isolines, we will define the segregation rate

as $\frac{dy_c^*}{dt}$ with y_c^* the elevation corresponding to the isoconcentration C .

A number of theories (May et al., 2010; Savage and Lun, 1988) have proposed a linear

dependence of the segregation rate to the shear rate defined as $\dot{\gamma} = \frac{dUp_x}{dy}$:

$$\frac{dy_c^*}{dt} \propto -\dot{\gamma} \quad (2)$$

Recall that the streamwise velocity profile is characterized by an exponential decay:

$Up_x \propto e^{-y^*/\lambda}$ with λ the exponential decay constant (see semi-log plot in Figure 9).

This means that the shear rate - derivative of the velocity – also follows an exponential decay:

$$\dot{\gamma} \propto c_0 \cdot e^{y^*/\lambda} \text{ with } c_0 \text{ the shear rate at } y^*=0$$

$$\text{hence } \frac{dy_c^*}{dt} \propto -c_0 \cdot e^{y_c^*/\lambda} \quad (3)$$

Separating variables and integrating from time $t=0$ and initial position gives

$$y_c^* = -\lambda \log\left(\frac{t}{\lambda} c_0 + c_1\right) \text{ with } c_1 \text{ a constant of integration.}$$

$$\text{When } t \gg 1, c_1 \text{ is negligible and hence } y_c^* = -\lambda \log(t) + c_2 \quad (4)$$

We have seen that the experimental small particle concentration isolines decrease as a logarithmic function of time (see fitting in Figure 7 and equation 1): $y_c^* = -a \log(t) + b$.

Therefore, if the segregation rate actually linearly depends on the shear rate, the absolute value of the slope of the isolines, a , should be equal to λ , the slope of the velocity profile.

Let us test this assumption on our data. On one hand, recall (Table 2) that fitting on the lower isolines ($C=0.01, 0.02$ and 0.05) yielded a slope value ranging from 1.21 to 1.37 (mean of 1.27) in run S6 and from 1.95 to 2.13 (mean of 2.06) in run S20.

On the other hand, streamwise velocity profiles were fitted over the exponential domain (Figure 9) in the same y^* region where the three isolines evolve ($C=0.01, 0.02$ and 0.05). In run S6 for y^* between -3 and -0.5 the exponential decay constant λ equals 1.37 (coefficient of determination R^2 of 0.995). In run S20, for y^* between -5 and -2 this constant equals 2.11 (R^2 of 0.986).

Figure 9 Streamwise particle velocity U_{px} and best fit in the same y^* region where concentration isolines were fitted (see Fig.7). a) run S6 b) run S20

Therefore, the agreement between the exponential decay constant λ derived from the velocity profile and the time constant derived from the logarithmic decay of the concentration isolines is good with an average difference of only 8% in run S6 ($\lambda=1.37$ vs. $a=1.27$) and 2% in run S20 ($\lambda=2.11$ vs. $a=2.06$).

To conclude, the present analysis shows that the particle shear rate drives vertical segregation at first order in turbulent bedload transport. This result is similar to what has been obtained in dry granular flows (May et al., 2010; Savage and Lun, 1988). It suggests that the mechanisms observed in turbulent bedload transport are not different from the ones observed in dry granular flows. This size-segregation mechanism results from the relative displacement of grains between the granular layers. Following Savage and Lun (1988), the creation of holes in the granular media due to the shear rate, induces a net downward small particle flux linked with a higher probability for a small particle to fall into a hole than for a large one.

In addition, the parallel with dry granular flows suggests that the models designed for such flows could be used in the future to model size-segregation in turbulent bedload transport (Thornton et al., 2006; Tunuguntla et al., 2014). Similarly, the shear-rate dependence could be included in the segregation flux as described by May et al. (2010).

4.2 Penetration depth

An important question is whether there is a cut-off shear rate under which no kinetic sieving is possible. This would explain the constant values reached by the lower isolines and hence the possibility to define the ‘penetration depth’. Our experiments showed that no evolution of the penetration depth was observed after about 40 min in run S6 and 30 min in run S20. At this point, examination of the isolines gives a penetration depth of about $3D$ for S6 and $5D$ for S20.

This observation may be put into perspective with experimental or field measurements of infiltration resulting in maximum values of 2 to 5D₉₀ (with D₉₀ the diameter at which 90% of the coarse bed particle is finer). However, in field measurements, it is nearly impossible to distinguish between the evolution of the bedload layer and scour and fill phenomena due to bedform formation and travelling, notably bars, dunes and antidunes (Recking et al., 2009a). The depth of buried tracers is indeed the result of both phenomena. A discussion as how to distinguish and simply name both phenomena was provided by Church and Haschenburger (2017). Therefore, most investigations have been made in hydraulic flumes and, moreover, with stable gravel beds. For example, Beschta and Jackson (1979) reported infiltration down to 2.5–5D₉₀. Similar values were reported by Gibson et al. (2009), who underlined that the seal (called bridging) did not occur at a very definite elevation but that the fine content decayed exponentially with the depth. Whilst most field studies have reported infiltration due to the scour and fill process, some field experiments by Lisle (1989) were conducted over a relatively plane moving bed and resulted in a seal thickness of 2.6–3.6 D₉₀. To conclude, although the experimental conditions of our idealized experiments could at first sight be considered quite different from field conditions, the reported penetration depths have the same relative values.

However, since the velocity and the shear rate profiles are exponential, and if the proportionality assumption between the segregation rate and the shear rate still holds in the lowermost layers, simple theories such as Savage and Lun (1988) predict that the penetration depth should continue to evolve with no cutoff value. We recently conducted preliminary coupled fluid discrete simulations (Frey et al., 2017) that indeed showed no cutoff value for the penetration depth.

To summarize, we have two series of seemingly contradictory results. On the one hand, observations in the laboratory, including our idealized experiments, as well as in the field tend to show a maximal penetration depth. On the other hand, preliminary coupled fluid discrete

simulations and simple theories show no cutoff value of the penetration depth, with the system therefore never reaching a steady state.

Further comments can be made to reconcile these two observations. Since the granular shear rate exhibits an exponential decrease in the bed, the expected downward segregation motion of the small particles should scale with the logarithm of time. Therefore, the experimental duration might be too short to observe further motion. In the present case, roughly speaking, the time needed for a small particle to move down is ten times greater every length of the large diameter. It is therefore possible that our one hour long experiment needs to be run for considerably longer durations. Ten hours would be needed to possibly see an added one-large-diameter-long descent and hundred hours for two diameters. At present experiments of this duration would be very difficult, or even impossible, to arrange.

With respect to field observations, it should be kept in mind here that the system is idealized, considering only steady and uniform configurations in a bi-disperse granular bed. The large grain size distribution and the non-uniform conditions (Bacchi et al., 2014) observed in the field could have important effects. Further work is required to understand physical mechanisms in idealized bedload transport and extend the analysis to more complex and realistic cases.

4.3 High resolution dataset for model validation

Bedload transport is essentially modeled with engineering-oriented shallow water equations together with the Exner mass conservation equation and with a semi-empirical excess shear stress transport rate formula (e.g. formula of Meyer-Peter and Müller (1948) or Smart and Jaeggi (1983)). However, in this framework there is no information on the normal (vertical) direction which is crucial for the study of vertical size segregation. More recently, Lagrangian discrete element models coupled with fluid solvers have been applied to bedload (Maurin et al.,

2018; Maurin et al., 2015). Likewise, continuous Eulerian two phase flow models have been developed with the use of an appropriate granular rheology (Cheng et al., 2018). Multiphase continuum models and multi-sized fluid-coupled discrete element models are now under development. It is therefore crucial to have high resolution spatio-temporal datasets to be able to validate those models. The dataset described in this paper can fulfil this goal.

5. CONCLUSION

We have analyzed the temporal evolution of new kinetic sieving experiments following the introduction of a low rate of smaller particles in a larger particle bedload flow at transport equilibrium. Segregation results in the progressive development of a quasi-continuous region of small particles reaching a steady-state penetration depth with time. Image processed concentration-depth profiles and isolines showed a logarithmic time decrease. We demonstrated that this evolution was dependent at first order on the streamwise shear rate at the bottom of the small particle region, which decays downwards exponentially. This result is in line with several theories originally developed for dry granular flows. However, this theory does not allow the system to reach a maximal constant penetration depth as evidenced by our experimental data as well by other field or experimental data. Further research is therefore necessary to reconcile these two observations. Finally, this high resolution spatio-temporal dataset could be used to develop and validate multi-size fluid coupled discrete element models as well as Eulerian multiphase models.

ACKNOWLEDGEMENTS

The work was funded by ‘Agence nationale de la recherche’ project SegSed ANR-16-CE01-0005. The work was also partly funded by the French “Institut National des Sciences de l’Univers” programme EC2CO-BIOHEFECT/DRIL and LabEx OSUG@2020

(Investissements d'avenir – ANR10 LABX56). The authors acknowledge the support of Irstea (formerly Cemagref). H. Lafaye de Micheaux also acknowledges funding provided by grants from la Région Rhône-Alpes. This work would not have been possible without the technical support of F. Ousset in the laboratory at Irstea.

REFERENCES

- Bacchi, V., Recking, A., Eckert, N., Frey, P., Piton, G., Naaim, M., 2014. The effects of kinetic sorting on sediment mobility on steep slopes. *Earth Surface Processes and Landforms* 39, 1075-1086, doi:10.1002/esp.3564.
- Bathurst, J. C., 2007. Effect of coarse surface layer on bed-load transport. *Journal of Hydraulic Engineering-Asce* 133, 1192-1205.
- Beschta, R. L., Jackson, W. L., 1979. Intrusion of Fine Sediments into a Stable Gravel Bed. *Journal of the Fisheries Research Board of Canada* 36, 204-210.
- Beucher, S., Lantuejoul, C., 1979. Use of watersheds in contour detection. *International Workshop on Image Processing : Real-time Edge and Motion Detection/Estimation*, Rennes.
- Bridgwater, J., Ingram, N. D., 1971. Rate of Spontaneous Inter-Particle Percolation. *Transactions of the Institution of Chemical Engineers* 49, 163-169.
- Capart, H., Fraccarollo, L., 2011. Transport layer structure in intense bed-load. *Geophysical Research Letters* 38, L20402, doi:10.1029/2011gl049408.
- Chauchat, J., 2018. A comprehensive two-phase flow model for unidirectional sheet-flows. *Journal of Hydraulic Research* 56, 15-28, doi:10.1080/00221686.2017.1289260.
- Cheng, Z., Hsu, T. J., Chauchat, J., 2018. An Eulerian two-phase model for steady sheet flow using large-eddy simulation methodology. *Advances in Water Resources* 111, 205-223, doi:10.1016/j.advwatres.2017.11.016.
- Church, M., Haschenburger, J. K., 2017. What is the "active layer"? *Water Resources Research* 53, 5-10, doi:10.1002/2016wr019675.
- Cui, Y., Wooster, J. K., Baker, P. F., Dusterhoff, S. R., Sklar, L. S., Dietrich, W. E., 2008. Theory of fine sediment infiltration into immobile gravel bed. *Journal of Hydraulic Engineering-Asce* 134, 1421-1429.
- Dermisis, D., Papanicolaou, A. N. T., 2014. The Effects of Protruding Rock Boulders in Regulating Sediment Intrusion within the Hyporheic Zone of Mountain Streams. *Journal of Mountain Science* 11, 1466-1477, doi:10.1007/s11629-014-3054-9.
- Drahn, J. A., Bridgwater, J., 1983. The Mechanisms of Free-Surface Segregation. *Powder Technology* 36, 39-53.
- DuBoys, M., 1879. Le Rhône et les rivières à lit affouillable. *Annales Ponts et Chaussées Serie 5, Vol XVIII*, 141-195.
- Dudill, A., Frey, P., Church, M., 2017. Infiltration of fine sediment into a coarse mobile bed: a phenomenological study. *Earth Surface Processes and Landforms* 42, 1171-1185, doi:10.1002/esp.4080.
- Dudill, A., Lafaye de Micheaux, H., Frey, P., Church, M., 2018. Introducing Finer Grains Into Bedload: The Transition to a New Equilibrium. *Journal of Geophysical Research: Earth Surface* 123, 2602-2619, doi:doi:10.1029/2018JF004847.
- Einstein, H. A., 1942. Formulas for the transport of bed sediment. *Trans. Am. Soc. Civ. Eng* 107, 561-574.

- Einstein, H. A., 1968. Deposition of suspended particles in a gravel bed. *Journal of the Hydraulics Division-Asce* 94, 1197-1205.
- Fan, Y., Hill, K. M., 2011. Theory for shear-induced segregation of dense granular mixtures. *New Journal of Physics* 13, 095009, doi:10.1088/1367-2630/13/9/095009.
- Ferdowsi, B., Ortiz, C. P., Houssais, M., Jerolmack, D. J., 2017. River-bed armouring as a granular segregation phenomenon. *Nature Communications* 8, 1363, doi:10.1038/s41467-017-01681-3.
- Frey, P., 2014. Particle velocity and concentration profiles in bedload experiments on a steep slope. *Earth Surface Processes and Landforms* 39, 646-655, doi:10.1002/esp.3517.
- Frey, P., Reboud, J. L., 2001. Experimental study of narrow free-surface turbulent flows on steep slopes. In: Ninokata, H., et al., (Eds.), *Advances in flow modeling and turbulence measurements*. World Scientific Publishing Co., Tokyo, 4-6 dec., pp. 396-403.
- Frey, P., Church, M., 2009. How River Beds Move. *Science* 325, 1509-1510.
- Frey, P., Church, M., 2011. Bedload: a granular phenomenon. *Earth Surface Processes and Landforms* 36, 58-69.
- Frey, P., Dufresne, M., Böhm, T., Jodeau, M., Ancey, C., 2006. Experimental study of bed-load on steep slopes. *River flow 2006*, Lisbonne, Portugal, 6-8 september. Balkema, pp. 887-893.
- Frey, P., Maurin, R., Morchid Alaoui, L., Gupta, S., Chauchat, J., 2017. Investigation of vertical size segregation in bedload sediment transport with a coupled fluid-discrete element model. *Powders and Grains Montpellier*, 3-7 July, France, EPJ Web of Conferences 140, 09025, <https://doi.org/10.1051/epjconf/201714009025>
- Frostick, L. E., Lucas, P. M., Reid, I., 1984. The Infiltration of Fine Matrices into Coarse-Grained Alluvial Sediments and Its Implications for Stratigraphical Interpretation. *Journal of the Geological Society* 141, 955-965.
- Gajjar, P., van der Vaart, K., Thornton, A. R., Johnson, C. G., Ancey, C., Gray, J. M. N. T., 2016. Asymmetric breaking size-segregation waves in dense granular free-surface flows. *Journal of Fluid Mechanics* 794, 460-505, doi:10.1017/jfm.2016.170.
- Gibson, S., Abraham, D., Heath, R., Schoellhamer, D., 2009. Vertical gradational variability of fines deposited in a gravel framework. *Sedimentology* 56, 661-676, doi:10.1111/j.1365-3091.2008.00991.x.
- Gibson, S., Heath, R., Abraham, D., Schoellhamer, D., 2011. Visualization and analysis of temporal trends of sand infiltration into a gravel bed. *Water Resources Research* 47, W12601, doi:10.1029/2011wr010486.
- Gilbert, G. K., 1914. The transportation of débris by running water, Professional paper 86, U.S. Geological Survey, Washington DC.
- Gomez, B., Church, M., 1989. An Assessment of Bed-Load Sediment Transport Formulas for Gravel Bed Rivers. *Water Resources Research* 25, 1161-1186.
- Gray, J. M. N. T., 2018. Particle Segregation in Dense Granular Flows. *Annual Review of Fluid Mechanics* 50, 407-433, doi:10.1146/annurev-fluid-122316-045201.
- Hergault, V., Frey, P., Métivier, F., Barat, C., Ducottet, C., Böhm, T., Ancey, C., 2010. Image processing for the study of bedload transport of two-size spherical particles in a supercritical flow. *Experiments in Fluids* 49, 1095-1107.
- Hill, K. M., Fan, Y., 2008. Isolating segregation mechanisms in a split-bottom cell. *Physical Review Letters* 101, 088001.
- Hinton, D., Hotchkiss, R. H., Cope, M., 2018. Comparison of Calibrated Empirical and Semi-Empirical Methods for Bedload Transport Rate Prediction in Gravel Bed Streams. *Journal of Hydraulic Engineering* 144, doi:10.1061/(asce)hy.1943-7900.0001474.

- Houssais, M., Ortiz, C. P., Durian, D. J., Jerolmack, D. J., 2015. Onset of sediment transport is a continuous transition driven by fluid shear and granular creep. *Nature Communications* 6, 6527, doi:10.1038/ncomms7527.
- Jain, N., Ottino, J. M., Lueptow, R. M., 2004. Effect of interstitial fluid on a granular flowing layer. *Journal of Fluid Mechanics* 508, 23-44.
- Lafaye de Micheaux, H., Ducottet, C., Frey, P., 2018. Multi-model particle filter-based tracking with switching dynamical state to study bedload transport. *Machine Vision and Applications* 29, 735-747, doi:10.1007/s00138-018-0925-z.
- Lafaye de Micheaux, H., Dudill, A. R., Frey, P., Ducottet, C., 2015. Image processing to study the evolution of channel slope and water depth in bimodal sediment mixtures. 10th Pacific Symposium on Flow Visualization and Image Processing, Naples, Italy, 15-18 June, No.43, https://www.psfvip10.unina.it/Ebook/web/papers/043_PSFVIP10.pdf.
- Lisle, T. E., 1989. Sediment Transport and Resulting Deposition in Spawning Gravels, North Coastal California. *Water Resources Research* 25, 1303-1319.
- Maurin, R., Chauchat, J., Frey, P., 2018. Revisiting slope influence in turbulent bedload transport: consequences for vertical flow structure and transport rate scaling (vol 839, pg 135, 2018). *Journal of Fluid Mechanics* 839, 693-693, doi:10.1017/jfm.2018.121.
- Maurin, R., Chauchat, J., Chareyre, B., Frey, P., 2015. A minimal coupled fluid-discrete element model for bedload transport. *Physics of Fluids* 27, 113302, doi:10.1063/1.4935703.
- May, L. B. H., Golick, L. A., Phillips, K. C., Shearer, M., Daniels, K. E., 2010. Shear-driven size segregation of granular materials: Modeling and experiment. *Physical Review E* 81, 051301, doi:10.1103/PhysRevE.81.051301.
- Meyer-Peter, E., Müller, R., 1948. Formulas for bed load transport. 2nd Congress of the International Association for Hydraulic Research, Vol. 2, Stockholm, pp. 39-64.
- Middleton, G. V., 1970. Experimental studies related to problems of flysch sedimentation. In: Lajoie, J., (Ed.), *Flysch Sedimentology in North America: Geological Association of Canada, Vol. Special Paper 7*, pp. 253-272.
- Parker, G., Klingeman, P. C., 1982. On Why Gravel Bed Streams Are Paved. *Water Resources Research* 18, 1409-1423.
- Recking, A., Bacchi, V., Naaim, M., Frey, P., 2009a. Antidunes on steep slopes. *Journal of Geophysical Research-Earth Surface* 114, F04025.
- Recking, A., Frey, P., Paquier, A., Belleudy, P., 2009b. An experimental investigation of mechanisms involved in bed load sheet production and migration. *Journal of Geophysical Research-Earth Surface* 114, F03010, doi:doi:10.1029/2008JF000990.
- Revil-Baudard, T., Chauchat, J., Hurther, D., Barraud, P. A., 2015. Investigation of sheet-flow processes based on novel acoustic high-resolution velocity and concentration measurements. *Journal of Fluid Mechanics* 767, 1-30, doi:10.1017/jfm.2015.23.
- Savage, S. B., Lun, C. K. K., 1988. Particle-Size Segregation in Inclined Chute Flow of Dry Cohesionless Granular Solids. *Journal of Fluid Mechanics* 189, 311-335.
- Smart, G. M., Jaeggi, M. N. R., 1983. Sedimenttransport in steilen Gerinnen. *Mitteilungen n°64 der Versuchanstalt für Wasserbau, Hydrologie und Glaziologie. ETH Zürich*, pp. 191.
- Soille, P., 1999. *Morphological image analysis : Principles and Applications*. Springer-Verlag Berlin Heidelberg
- Thornton, A. R., Gray, J., Hogg, A. J., 2006. A three-phase mixture theory for particle size segregation in shallow granular free-surface flows. *Journal of Fluid Mechanics* 550, 1-25.
- Tunuguntla, D. R., Bokhove, O., Thornton, A. R., 2014. A mixture theory for size and density segregation in shallow granular free-surface flows. *Journal of Fluid Mechanics* 749, 99-112, doi:10.1017/jfm.2014.223.

- van der Vaart, K., Gajjar, P., Epely-Chauvin, G., Andreini, N., Gray, J., Ancey, C., 2015. Underlying Asymmetry within Particle Size Segregation. *Physical Review Letters* 114, 10.1103, doi:10.1103/PhysRevLett.114.238001.
- Vincent, L., Soille, P., 1991. Watersheds in Digital Spaces: An Efficient Algorithm Based on Immersion Simulations. *IEEE Transactions on Pattern Analysis and Machine Intelligence* 13, 583-598, doi:10.1109/34.87344.
- Warburton, J., 1992. Observations of Bed-Load Transport and Channel Bed Changes in a Proglacial Mountain Stream. *Arctic and Alpine Research* 24, 195-203.
- Wiederseiner, S., Andreini, N., Epely-Chauvin, G., Moser, G., Monnereau, M., Gray, J. M. N. T., Ancey, C., 2011. Experimental investigation into segregating granular flows down chutes. *Physics of Fluids* 23, 013301, doi:10.1063/1.3536658.
- Wu, B., Nevatia, R., 2007. Detection and tracking of multiple, partially occluded humans by Bayesian combination of edgelet based part detectors. *International Journal of Computer Vision* 75, 247-266, doi:10.1007/s11263-006-0027-7.

List of figures

Figure 1: Scheme of the experimental device (modified from Hergault et al. 2010). The x-y coordinate system is shown. Note that the origin is taken at the top of the downstream obstacle

Figure 2: Steps of the object detection process. (a) original image, (b) thresholding to keep only black pixels, (c) eroding to isolate black beads, (d) detecting the center of the individual connected components being the black bead centers, (e) erasing black beads, (f) transforming by *hconvex*, (g) correlating with a ring-shaped model, (h) selecting maximal correlation results as being the transparent bead centers.

Figure 3: Sequence of images showing the temporal evolution of the segregation patterns in run S6 (a-f) and run S20 (g-l). Superimposed trajectories appear on panel b (over a prior duration of 38s) and f (over a prior duration of 6 min only for beads still present in the image).

Figure 4: Depth structure of the initial one-size bedload flow (black square for S6 and red diamond for S20) a) particle velocity (with semi-log inset showing exponential decay) b) solid volume concentration c) particle transport rate

Figure 5: Temporal evolution of the small particle volume concentration depth profiles a) run S6 b) run S20. The median time of the temporal sequence is used in the legend. Axis scaling is the same but note a translation of 1 diameter D on the y-axis from S6 (-4.5 to 1) to S20 (-5.5 to 0)

Figure 6: Upper (light green) and lower (dark red) isolines of concentration for constant values of 0.01, 0.02, 0.05 and 0.1 (from outer to inner curve) a) run S6 b) run S20. Axis scaling is the same but note a translation of 1 diameter D on the y-axis from S6 (-4.5 to 1) to S20 (-5.5 to 0)

Figure 7: Lower isolines of concentration for constant values of 0.01, 0.02, 0.05 and 0.1 (from bottom to top) showing a logarithmic time evolution until about 1,000s. A best fit is plotted for 0.01, 0.02 and 0.05 isolines a) run S6 b) run S20. Axes scaling is the same but note a translation of 1 diameter D on the y-axis from S6 (-4.5 to -1) to S20 (-5.5 to -2)

Figure 8: Temporal evolution of normal small particle velocity depth profiles a) run S6 b) run S20. The median time of the temporal sequence from time 0 is used in the legend.

Figure 9: Streamwise particle velocity U_{px} and best fit in the same y^* region where concentration isolines were fitted (see Figure 6). a) run S6 b) run S20

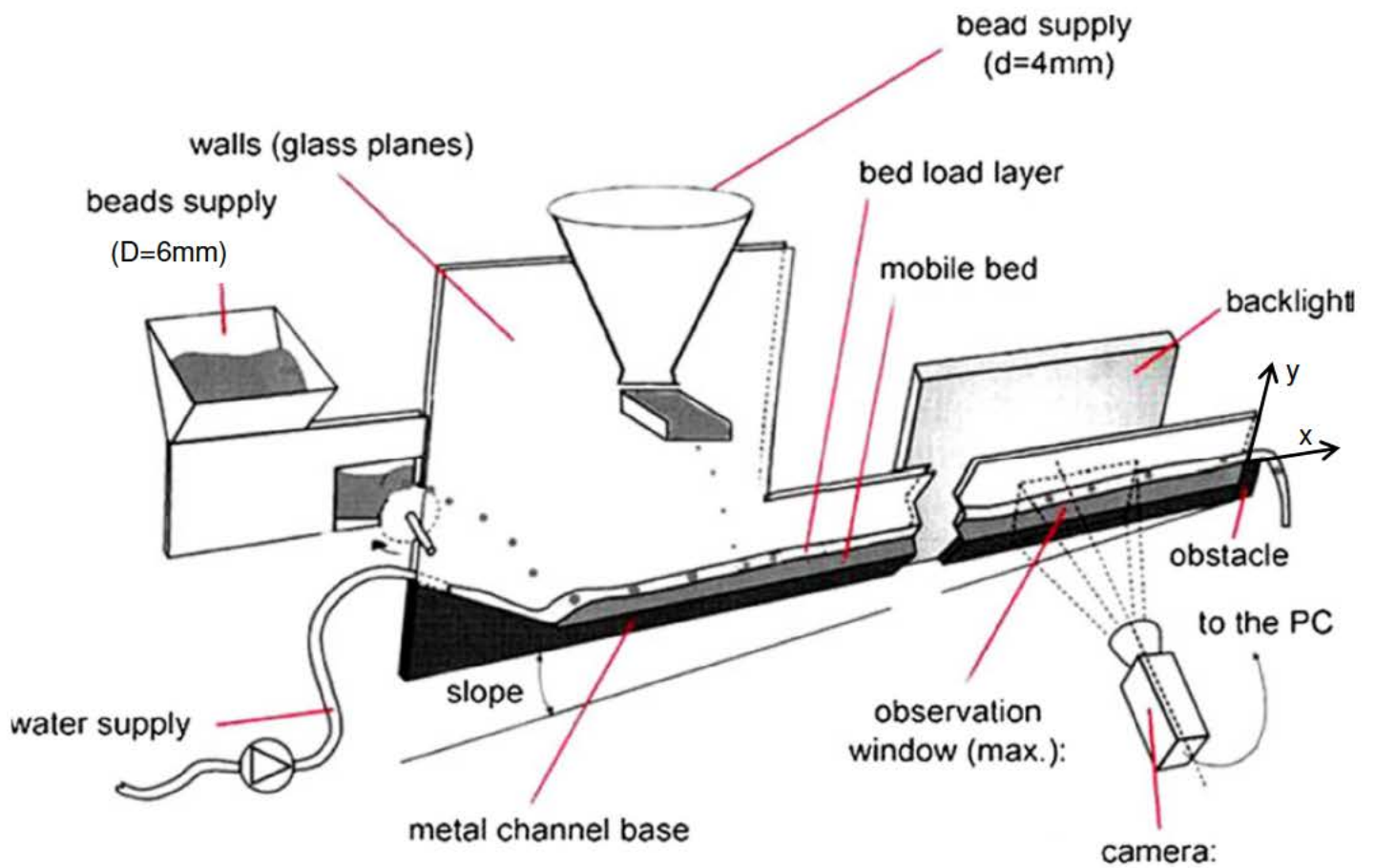


Figure 1 : Scheme of the experimental device (modified from Hergault et al. 2010). The x-y coordinate system is shown. Note that the origin is taken at the top of the downstream obstacle

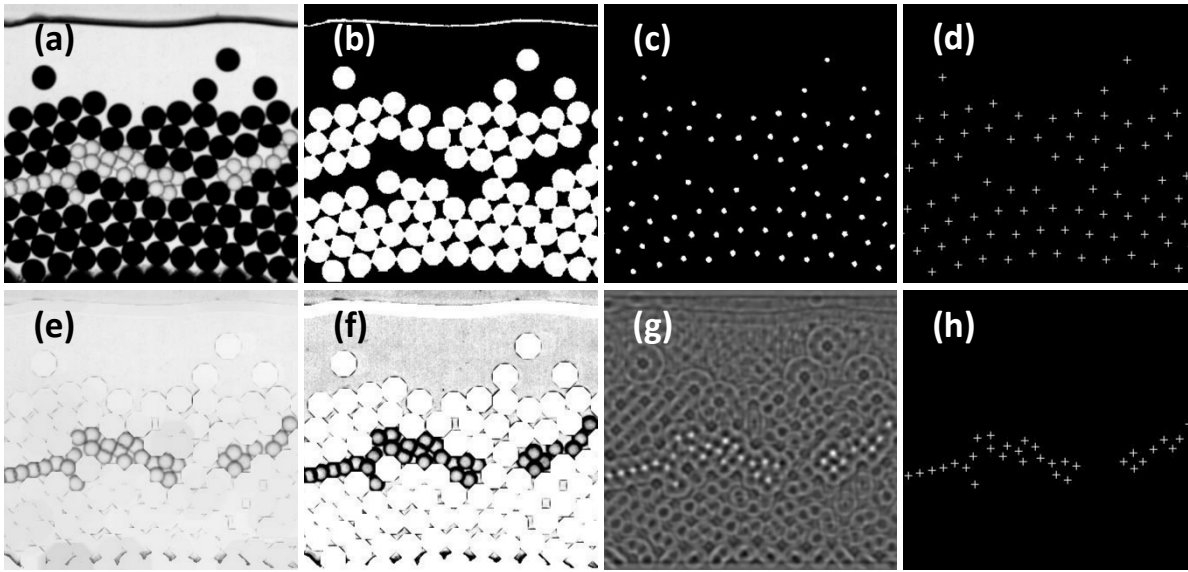


Figure 2 : Steps of the object detection process. (a) original image, (b) thresholding to keep only black pixels, (c) eroding to isolate black beads, (d) detecting the center of the individual connected components being the black bead centers, (e) erasing black beads, (f) transforming by *hconvex*, (g) correlating with a ring-shaped model, (h) selecting maximal correlation results as being the transparent bead centers.

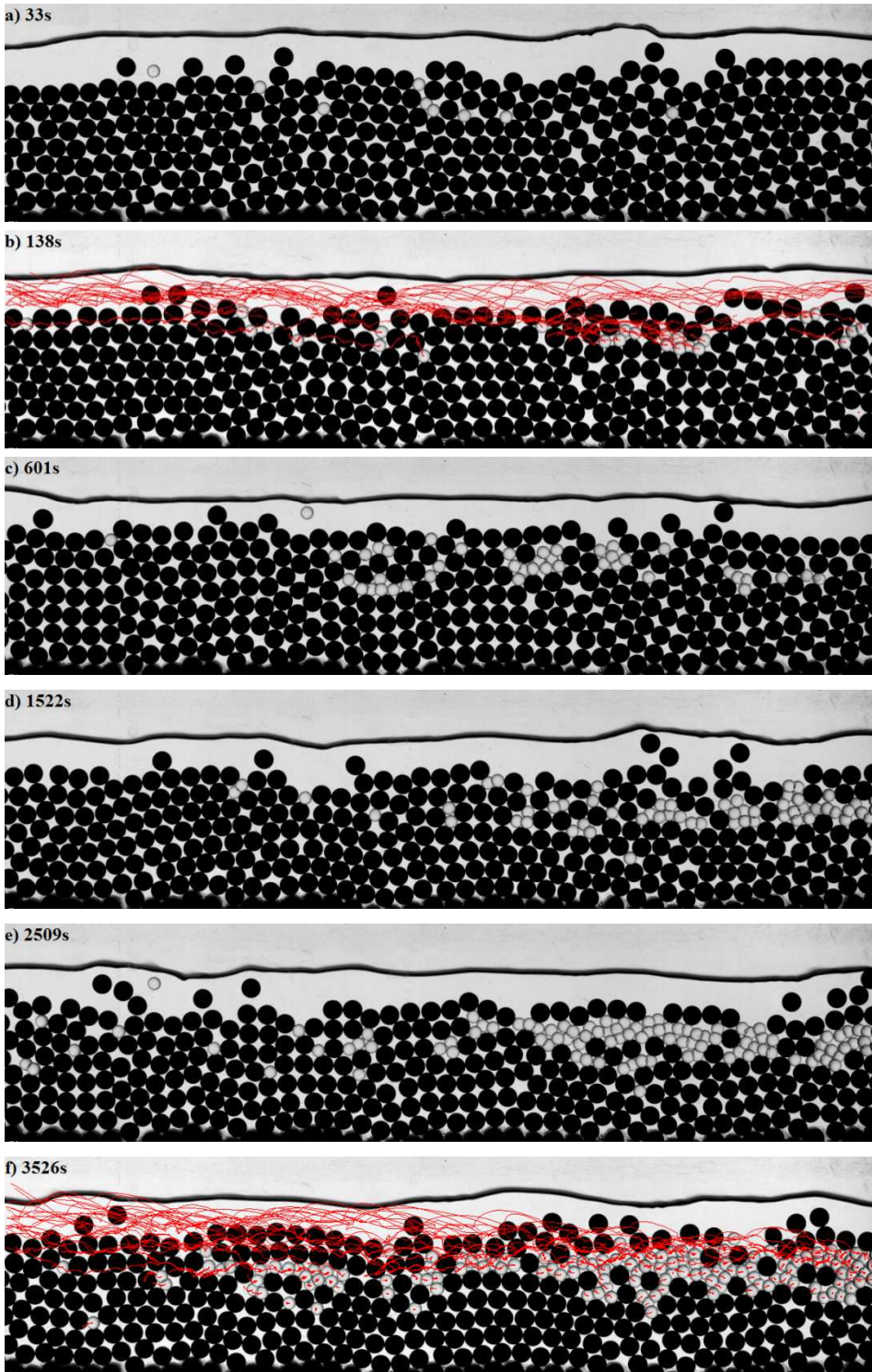


Figure 3 Sequence of images showing the temporal evolution of the segregation patterns in run S6 (a-f) and run S20 <next page> (g-l). Superimposed trajectories appear on panel b (over a prior duration of 38s) and f (over a prior duration of 6 min only for beads still present in the image).

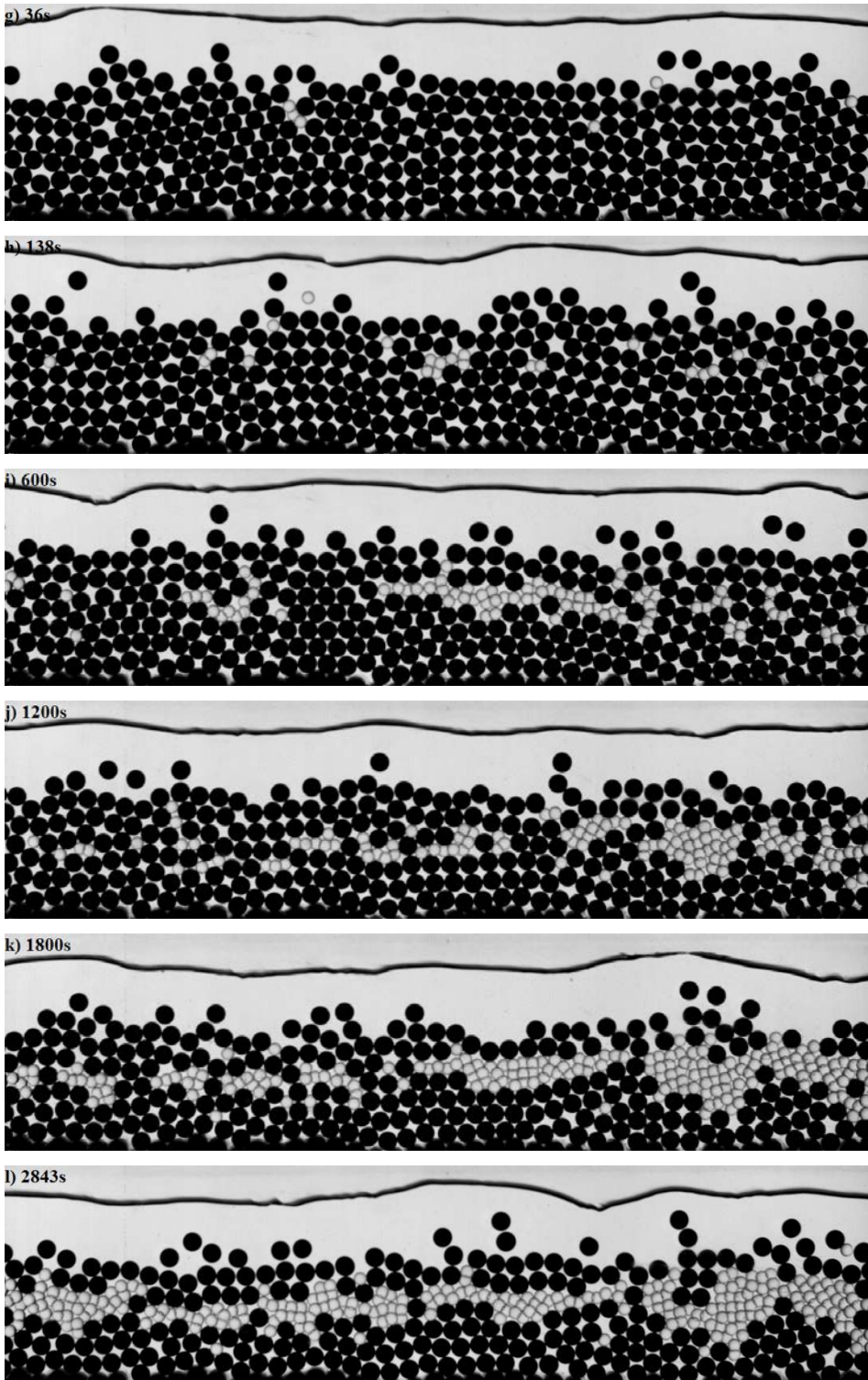


Figure 3 : continued

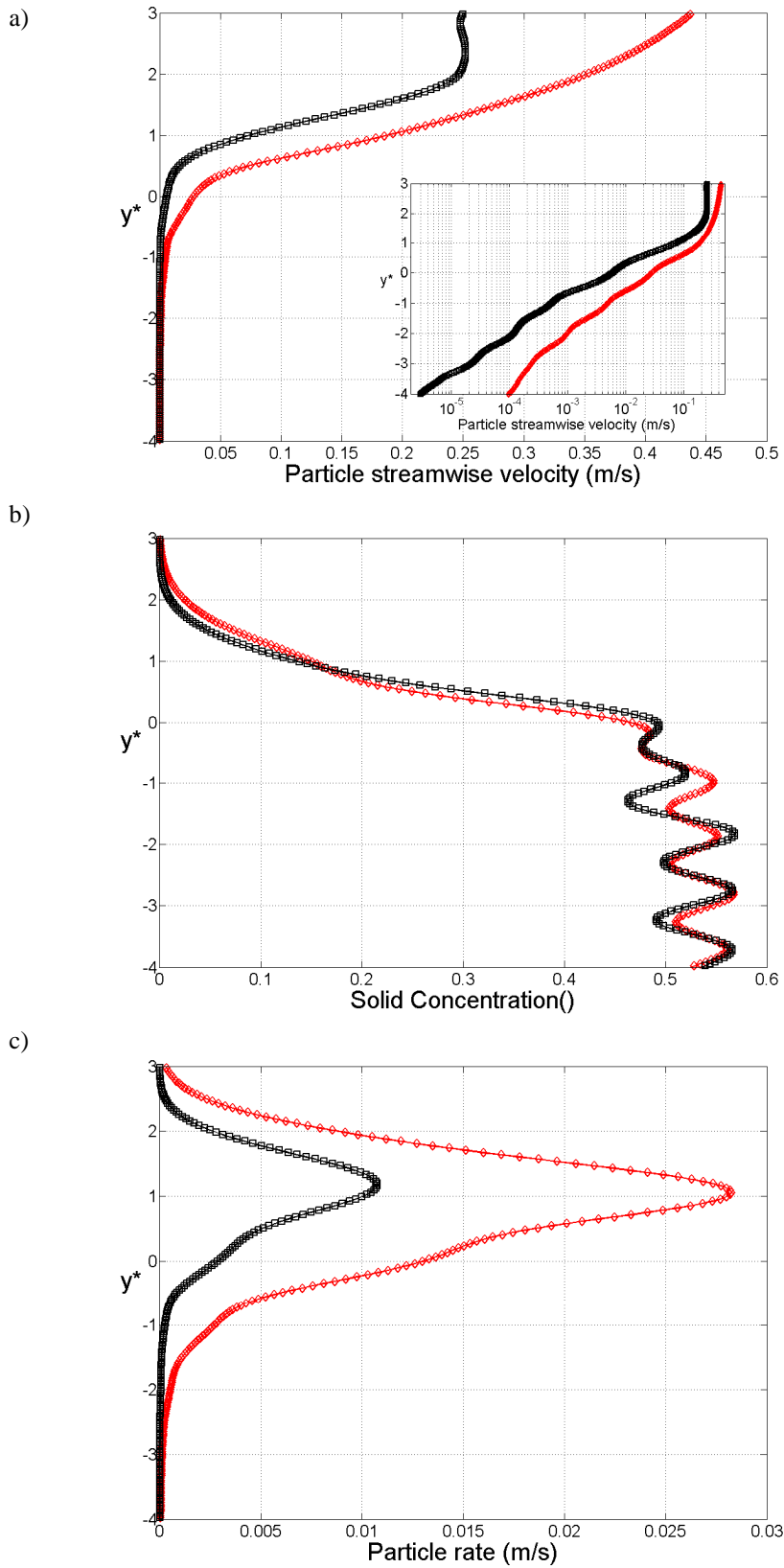
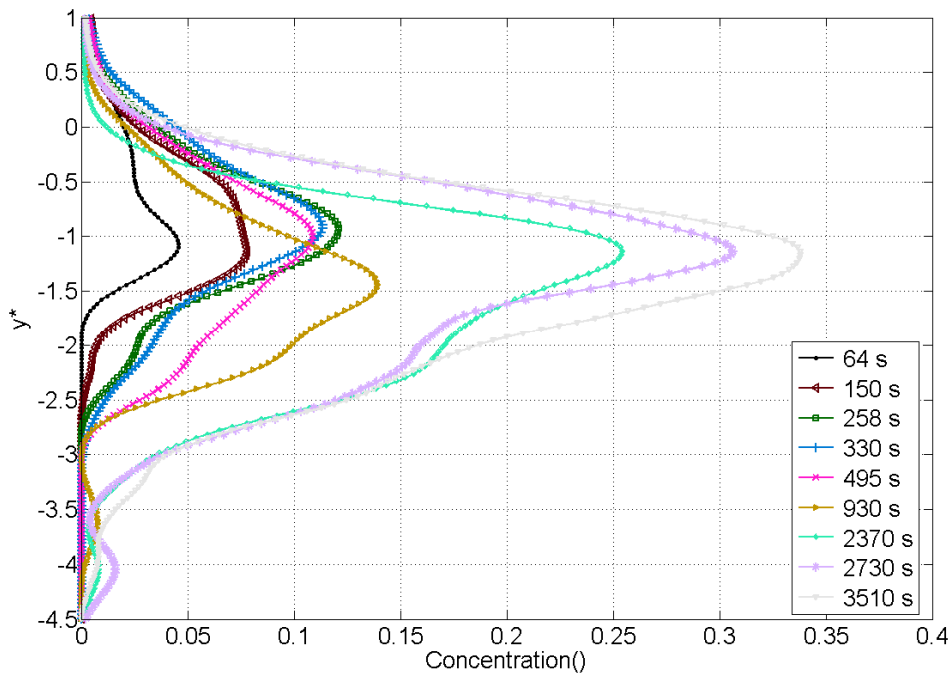


Figure 4 : Depth structure of the initial one-size bedload flow (black square for S6 and red diamond for S20) a) particle velocity (with semi-log inset showing exponential decay) b) solid volume concentration c) particle transport rate

a)



b)

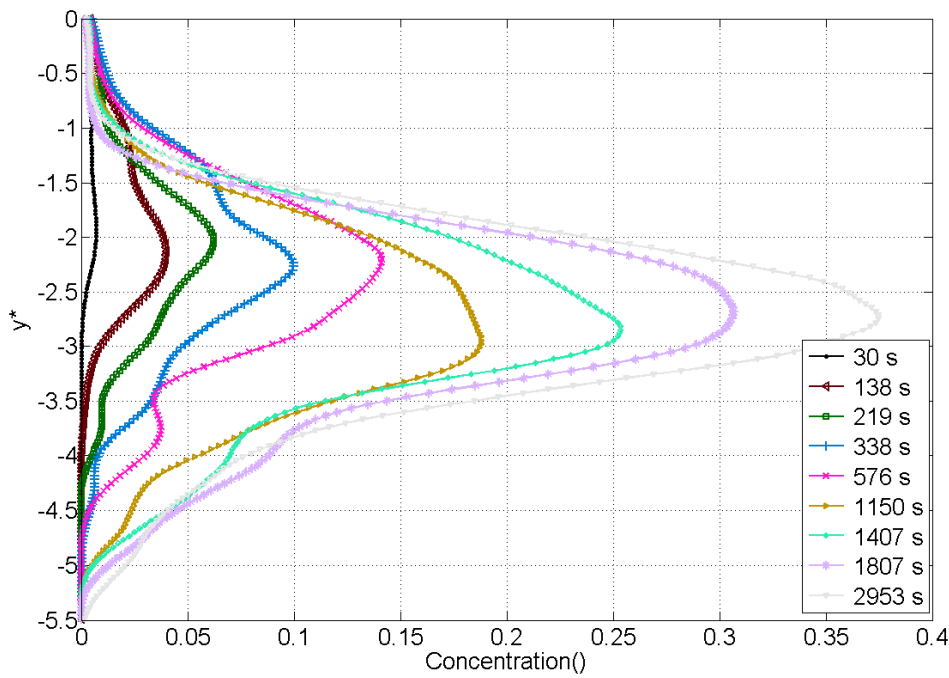


Figure 5 : Temporal evolution of the small particle volume concentration depth profiles a) run S6 b) run S20. The median time of the temporal sequence is used in the legend. Axis scaling is the same but note a translation of 1 diameter D on the y -axis from S6 (-4.5 to 1) to S20 (-5.5 to 0)

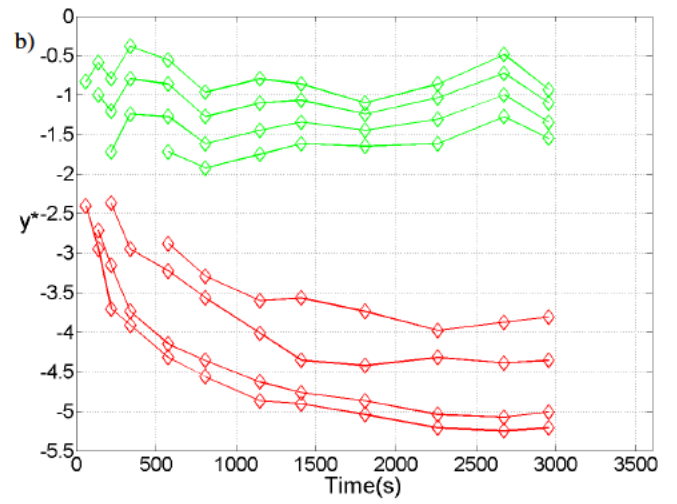
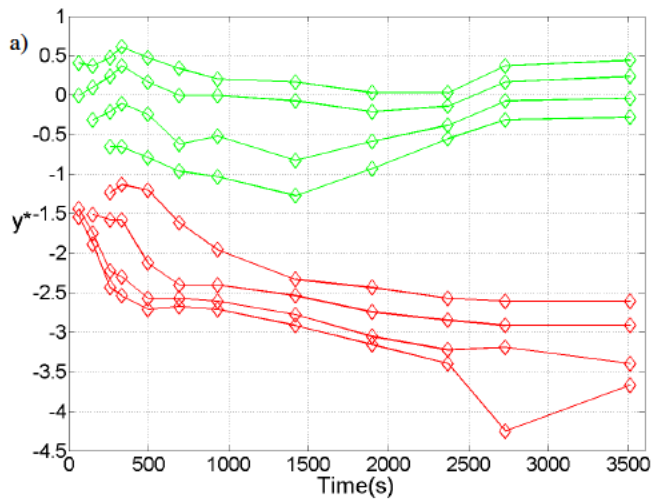


Figure 6 : Upper (light green) and lower (dark red) isolines of concentration for constant values of 0.01, 0.02, 0.05 and 0.1 (from outer to inner curve a) run S6 b) run S20. Axis scaling is the same but note a translation of 1 diameter D on the y -axis from S6 (-4.5 to 1) to S20 (-5.5 to 0)

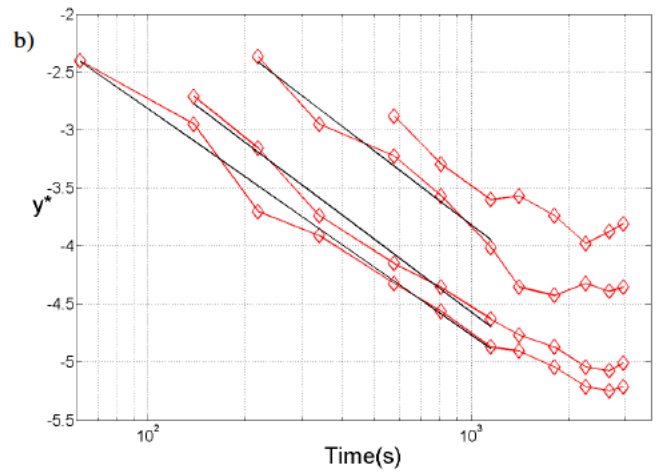
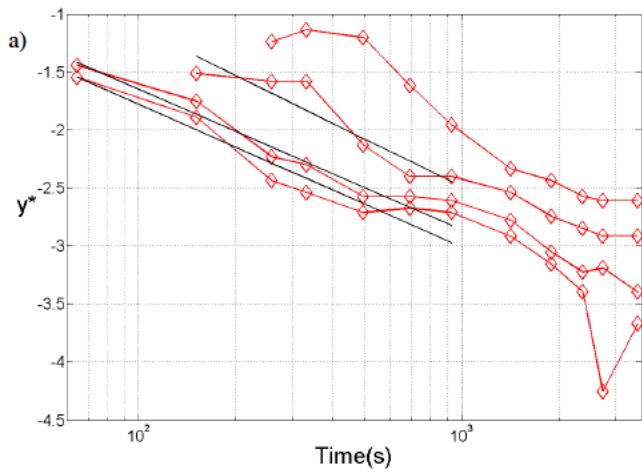
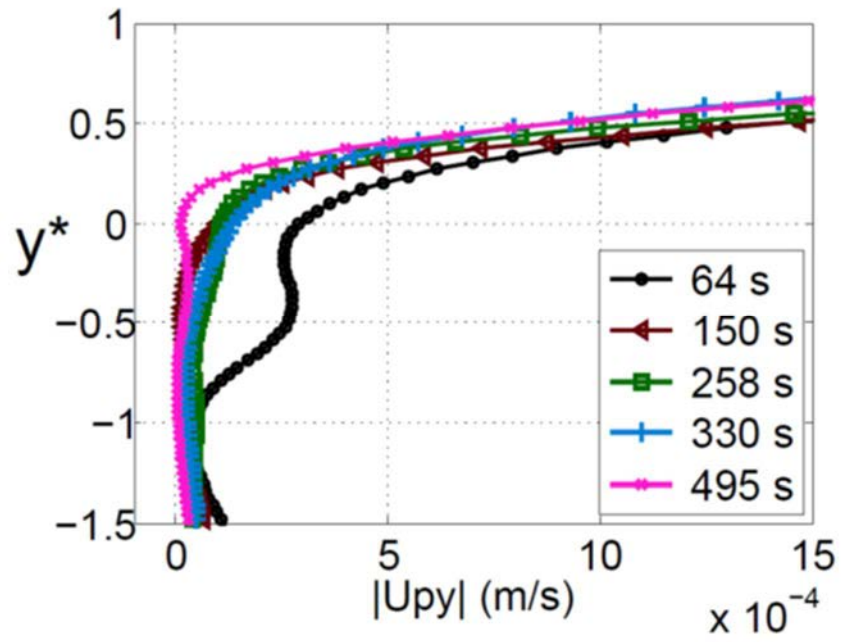


Figure 7 : Lower isolines of concentration for constant values of 0.01, 0.02, 0.05 and 0.1 (from bottom to top) showing a logarithmic time evolution until about 1,000s. A best fit is plotted for 0.01, 0.02 and 0.05 isolines a) run S6 b) run S20. Axes scaling is the same but note a translation of 1 diameter D on the y -axis from S6 (-4.5 to -1) to S20 (-5.5 to -2)

a)



b)

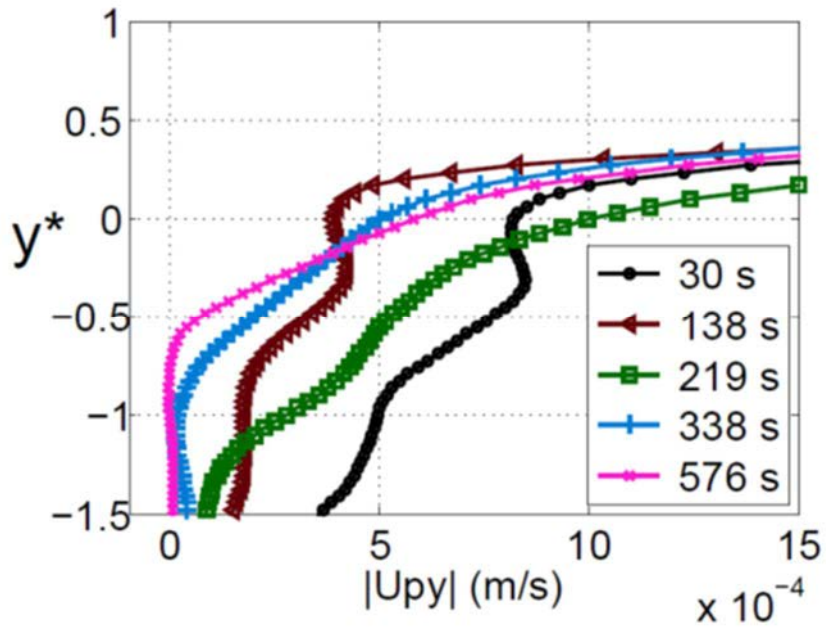


Figure 8 : Temporal evolution of normal small particle velocity depth profiles a) run S6 b) run S20. The median time of the temporal sequence from time 0 is used in the legend.

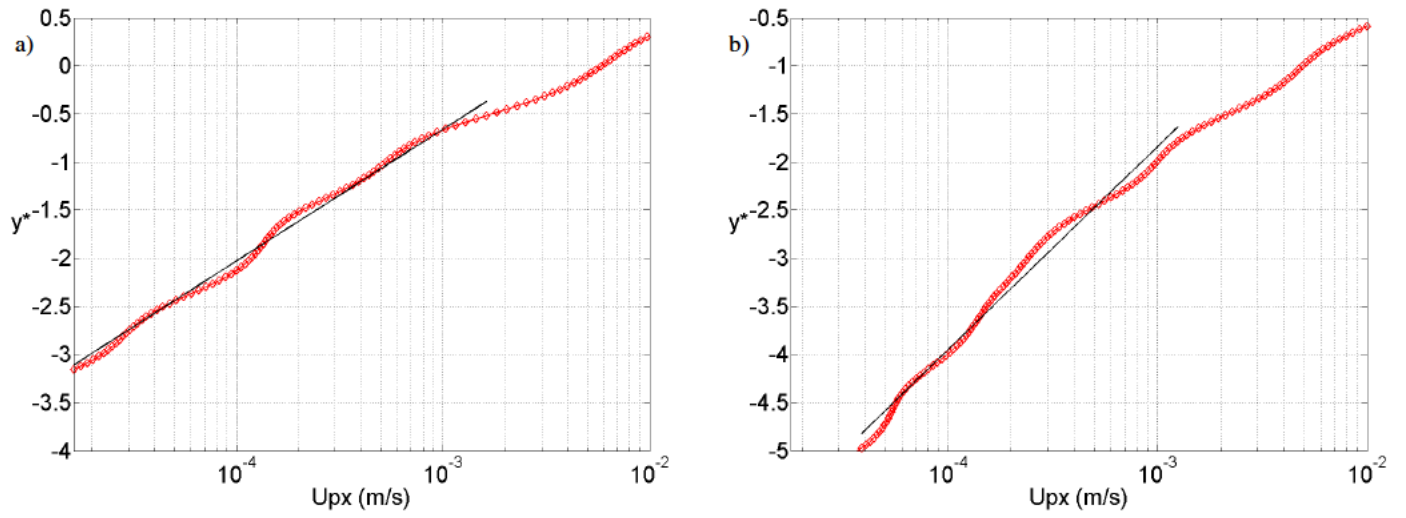


Figure 9 : Streamwise particle velocity U_{px} and best fit in the same y^* region where concentration isolines were fitted (see Figure 7). a) run S6 b) run S20